Pressure-induced instabilities in bulk TiO_2 rutile

2004 J. Phys.: Condens. Matter 16 273

(http://iopscience.iop.org/0953-8984/16/3/008)

INSTITUTE OF PHYSICS PUBLISHING JOURNAL OF PHYSICS: CONDENSED MATTER

J. Phys.: Condens. Matter **16** (2004) 273–292 PII: S0953-8984(04)67737-X

Pressure-induced instabilities in bulk TiO_2 rutile

B Montanari and N M Harrison

Chemistry Department, Imperial College of Science Technology and Medicine, South Kensington, London SW7 2AZ, UK

Received 18 August 2003
Published 9 January 2004
Online at stacks.iop.org/JPhysCM/16/273 (DOI: 10.1088/0953-8984/16/3/008)

Abstract

Density functional calculations, within the local density approximation, are used to investigate the isotropic pressure dependence of the geometry and Γ-point phonons of TiO_2 rutile over the range -8.6–8.6 GPa. The TO A_{2u} mode, which is the c-axis ferroelectric mode, vanishes at $P \sim -4$ GPa, thereby leading to a crystal instability and a possible ferroelectric phase transition. The effects of a uniaxial strain along the c-axis on the geometry and the TO A_{2u} mode are also investigated. This mode vanishes when the lattice parameter along c is just over 3% larger than in the unstrained case, again leading to a ferroelectric phase transition. Based on this result, it is suggested that expanded rutile structures might be created with enhanced dielectric properties by, for instance, thin film growth on a substrate with a small lattice mismatch. The microscopic origin of the ferroelectric stabilization is investigated and shows similarities with the case of perovskite oxides. The Raman-active B_{1g} mode unusually softens as the pressure increases and the atomistic origin of this behaviour is explained. The critical pressure for the second-order phase transition to a $CaCl_2$-type structure induced by this softening (when combined with an orthorhombic distortion) is calculated to be 13 GPa. The results for the pressure dependence of the geometry and lattice dynamics agree well with the available measured data.

1. Introduction

The dielectric constants of TiO_2 rutile are unusually high for a material of its class and make it very useful in many areas of application. Despite their name, the dielectric constants vary when varying physical conditions such as, for instance, pressure and temperature. Knowing their temperature and pressure dependence helps rationalize and tune the performance of this material in technological applications. Several experimental investigations have analysed the influence of pressure and temperature on the dielectric properties of TiO_2 rutile. Parker [1], for instance, measured the variation of the static dielectric constants of rutile at values of temperature between 1.6 and 1060 K. She found that they increase dramatically as the temperature decreases. Normally, this behaviour occurs on the approach of a temperature-driven ferroelectric phase transition. In this case, however, the temperature reaches 0 K

before the ferroelectric transition occurs. Thereby, TiO_2 rutile is classified as an *incipient ferroelectric*. Subsequently, measurements of the vibrational spectra [2, 3] explained the origin of this property at the atomistic scale. These studies clearly evidenced a link between the temperature dependence of the *c*-axis dielectric constant and the softening of the transverse optic (TO) A_{2u} vibrational mode of the atoms as the temperature decreases.

$KTaO_3$ and $CaTiO_3$ are also incipient ferroelectric materials. Postnikov *et al* [4] showed, based on the full-potential linear muffin-tin orbital method, that an isotropic expansion of the volume of $KTaO_3$ leads to the stabilization of the Ta atom in an off-centre position, thereby inducing a ferroelectric instability. Wang *et al* [5] performed first-principles calculations on $CaTiO_3$ and showed that the ferroelectric phase is favoured over the paraelectric one if the cell volume is isotropically expanded by 10%. In the present paper it will be shown that in a similar way a ferroelectric instability can be induced in TiO_2 rutile by applying a negative isotropic pressure and the critical pressure for the ferroelectric phase transition will be quantified. Both $KTaO_3$ and $CaTiO_3$ are perovskite oxides and hence inherently different from the rutile system investigated here. Therefore this work shows that the possibility of inducing a ferroelectric phase transition by applying negative isotropic pressure is not specific of the perovskite structure only. Also, the microscopic origin for the pressure-induced stabilization of the ferroelectric phase in rutile will be investigated and conclusions will be drawn about similarities and differences between this case and the origin of this phenomenon in the perovskite oxides.

In addition, it will be shown that in the case of rutile the ferroelectric phase can be stabilized also by applying *anisotropic* negative pressure, more specifically uniaxial strain. To the authors' best knowledge, the possibility of inducing a ferroelectric phase transition in an incipient ferroelectric by applying uniaxial strain has not been previously reported. This result may have important technological consequences. Whilst it is difficult to produce isotropically expanded samples of these materials, uniaxially strained lattices can be produced by growing them as thin films on a substrate with a small lattice mismatch. The calculations reported here suggest that a compression by just 1% of the lattice constants in the *a*–*b* plane of rutile is sufficient to trigger the ferroelectric phase transition and a compression by 0.8% already produces a ten-fold increase in its *c*-axis dielectric constant. These results therefore suggest that by controlled epitaxial growth rutile can be produced in thin films with a dielectric constant enhanced at will and can thus be tailored for technological applications.

All results in this work are obtained via calculations, based on density functional theory (DFT), of the Γ-point lattice dynamics of rutile over a range of either hydrostatic pressures or uniaxial strains. Recently, Dubrovinsky *et al* [10] discovered, by means of *ab initio* calculations in conjunction with experiment, the existence of a new crystalline phase of TiO_2 rutile, called cotunnite, which is the hardest known oxide. This confirms the predictive power of *ab initio* calculations and the important role played by the combination of modelling and experiment.

To the authors' knowledge, no theoretical investigation, using either empirical potentials or electronic structure methods, of the effects of pressure on the atomic vibrations of rutile has been reported yet. At zero pressure, both rigid-ion models [2] and shell models [11] have been used to investigate the vibrational properties of rutile. However, despite a great deal of research, including the recent use of variable charge models, it has not been possible to generate a transferable model of titania which simultaneously reproduces its structural, dielectric and vibrational properties [12, 13]. Lee *et al* [14] used a variational approach to DFT, within the local density approximation (LDA) to the exchange–correlation energy, to compute the Γ-point vibrational modes, the dielectric tensor and the Born effective charges of bulk TiO_2 rutile at zero pressure. The resulting phonon frequencies agree with experiment to within a few per cent. Our recent report [15] confirmed this result and explored the influence of more sophisticated

approximations than LDA on the Γ-point phonons of rutile at zero pressure. It was found that the gradient-corrected functionals PW91 [16] and the PBE [17], which generally lead to an improvement of ground-state energetics in solids, are much less accurate compared to LDA in the prediction of the Γ-point vibrational frequencies of rutile at zero pressure.

The present calculations, performed within LDA, provide the pressure dependence of *all* Γ-point phonons of rutile. Among them, only the B_{1g} mode unusually softens as the pressure increases. This phenomenon generally hints at the onset of a mode instability and there has been debate in the past as to whether this observation explains pressure-induced transformations of rutile [3, 18–24]. Nagel and O'Keeffe [18] noticed that the atomic displacements associated with this mode transform the rutile structure into a $CaCl_2$-type structure and suggested that this is the transformation observed by Nicol and Fong [19]. Later, Mammone *et al* [21] proved, based on factor group analysis, that the phase detected by Nicol and Fong cannot have the $CaCl_2$-type structure. In fact the experimental studies performed so far [21–24] have shown that TiO_2 rutile undergoes a sluggish phase transformation to the columbite structure (α-PbO_2-type) over a broad range of pressure (5–12 GPa) and no evidence of a rutile to $CaCl_2$ transition has been seen. On the theoretical side, computational investigations of TiO_2 under pressure have been performed based on either empirical atomistic methods [12] or more detailed *ab initio* electronic structure calculations [25]. In these studies, however, the $CaCl_2$-type structure was not considered.

In SiO_2, the B_{1g} mode also softens when increasing the pressure and this does cause a phase transition from stishovite, which has the rutile structure, to the $CaCl_2$-type structure at about 50 GPa [26, 27]. In addition, this transformation of stishovite is known to be of second order [28]. Concerning TiO_2, there has been a debate as to whether a phase transition from rutile to a $CaCl_2$-type would be of first or second order [3, 18, 21–23]. In the present paper the origin of the softening of the B_{1g} mode with increasing pressure is analysed and the critical pressure for the structural instability related to this mechanism is calculated. Furthermore, conclusions about the nature of the possible phase transition to a $CaCl_2$-type structure driven by this mode are drawn.

In the following section of this paper, details of the computational method are illustrated. The changes in the structural parameters induced by hydrostatic pressure and by uniaxial strain applied along the *c*-axis are examined in sections 3.1 and 3.2, respectively. In section 3.3 the hydrostatic pressure dependence for all Γ-point vibrational modes is presented. Sections 3.4 and 3.5 report the softening of the TO A_{2u} mode and the consequent ferroelectric phase transition induced by hydrostatic pressure and uniaxial strain, respectively. The atomistic origin of the ferroelectric stabilization is investigated in section 3.6. The softening of the Raman-active B_{1g} mode with increasing positive hydrostatic pressure and the nature of the possible phase transition related to this mechanism are discussed in section 3.7. Finally, all findings are summarized and final remarks are drawn in section 4.

2. Computational method

The present calculations are based on a plane-wave pseudopotential implementation of density functional theory [29, 30] and use the CASTEP [31] program. A number of calculations are repeated using the CRYSTAL [32] software package, where the crystalline orbitals are expanded as a linear combination of atom-centred Gaussian orbitals (LCAO) with s, p or d symmetry. CRYSTAL is used here for all electron calculations, i.e. with no shape approximation to the electronic charge density or ionic potential. The comparison of the CASTEP and CRYSTAL results is used to verify that the results are independent of the particular numerical scheme used to implement DFT. For both CASTEP and CRYSTAL,

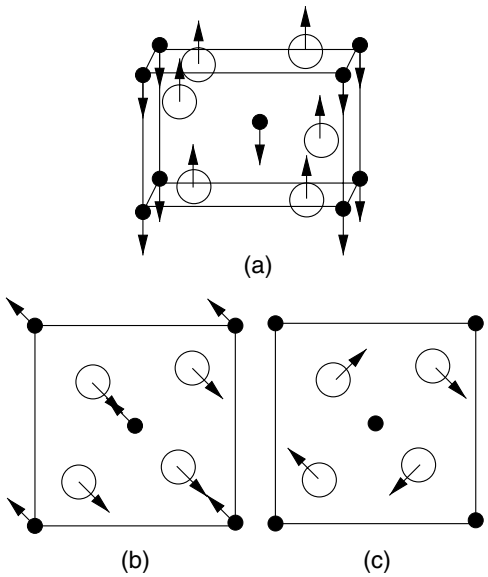

Figure 1. Atomic displacements associated with the eigenvectors relative to the A_{2u} (a), softest E_u (b) and B_{1g} (c) modes. Full and empty circles represent the Ti and O atoms, respectively. In (a) the vertical axis is the *c*-axis, whilst in (b) and (c) the *c*-axis is perpendicular to the plane of the figure.

the details of the calculations are given elsewhere [15]. The LDA functional, which relies on accurate calculations of the exchange–correlation density in a homogeneous electron gas, is selected for the present calculations. As shown elsewhere [15], this functional is an excellent choice and should be preferred to gradient-corrected functionals such as PW91 [16] and PBE [17], for describing the vibrational properties of TiO_2 rutile. The implementation of LDA chosen for the present work follows the recipe due to Ceperley and Alder [33].

The rutile structure, shown in figure 1(a), is primitive tetragonal (D_{4h}^{14}, $P4_2/mnm$) with six atoms per primitive unit cell. The two titanium atoms occupy positions (000) and $(\frac{1}{2}\frac{1}{2}\frac{1}{2})$, and the four oxygen atoms occupy positions $\pm(uu0)$ and $\pm(\frac{1}{2}+u, \frac{1}{2}-u, \frac{1}{2})$. The calculations start from the atomic coordinates and lattice parameters determined from neutron diffraction data of the crystalline bulk system [34] at ambient pressure and are performed without constraint (on symmetry or otherwise) until the magnitude of the average force on the atoms is less than 0.02 eV $Å^{-1}$ and the change in total energy is less than 10^{-6} eV. Details of the calculations under isotropic and anisotropic pressure are given in sections 3.1 and 3.2, respectively. For the equilibrium geometry, the Γ-point vibrational harmonic frequencies and eigenvectors are calculated via the finite difference scheme described previously [15].

3. Results and discussion

3.1. The variation of the structure with isotropic pressure

A full geometry optimization is performed for the system subject to discrete values of hydrostatic pressure in the range −8.6–8.6 GPa. For any given value of pressure, P, all structural degrees of freedom are optimized, therefore giving the predicted equilibrium

Table 1. Parameters of the linear fit to several equilibrium structural parameters as a function of P: $f(P) = f_0 + f_1 P$. The parameters of the linear fit to the measured values [37] are given in brackets when available. O_1 and O_2 are the nearest and next nearest neighbours of the Ti atom, respectively.

Parameters	f_0	f_1 (10^{-3} GPa^{-1})
a (Å)	4.551 (4.593)	−7.73 (−8.62)
c (Å)	2.920 (2.957)	−2.41 (−2.14)
u	0.3040	−0.14
c/a (Å)	0.642 (0.644)	0.56 (0.79)
Ω (Å^3)	60.500 (62.384)	−255.71 (−281.75)
Ti–O_1 (Å)	1.929	−1.70
Ti–O_2 (Å)	1.956	−4.27

geometry, by minimizing the enthalpy function H:

$$H = E + P\Omega, \tag{1}$$

with respect to all structural degrees of freedom. Here, E is the internal energy of the system and Ω is the unit cell volume. A plot of the total energy as a function of the equilibrium unit cell volume, Ω, was reported earlier [15] and gives a bulk modulus of 234.4 GPa, which is in excellent agreement with previous LDA calculations [25] and compares fairly well with experiment [35, 36]. Here, the equilibrium values for a, c and u against pressure are plotted, together with the measured values [37], in figure 2. All calculated quantities are very close to the experiment, although slightly underestimate it, over the whole P range. This is in line with the general tendency of LDA to underestimate equilibrium volumes. In addition, the measurements reported here were performed at room temperature. As reported previously [15], the LDA equilibrium geometry is in particularly good agreement with that measured at low T [34]. In order to highlight trends and for a more quantitative comparison with experiment, a linear fit $f(P) = f_0 + f_1 P$ of each structural parameter was performed. The results for a, c and u are reported in figure 2, which shows that the assumption of a nearly linear P dependence is justified. The resulting values of f_0 and f_1 for a, c, u, c/a, Ω and Ti–O bond distances are reported in table 1. The dependence for a, c and Ω compares very well with the measured dependence, provided that we discard the measured value of c at $P = 7.6$ GPa, which lies outside the line that fits well all other experimental data. The calculated pressure dependence is in particularly good agreement with that measured at low T. For instance, the volume compressibility, $\kappa = -(\frac{\partial \ln \Omega}{\partial P})_T$, derived from our data is equal to 4.22×10^{-3} GPa^{-1}. Samara and Peercy [3] found $\kappa = 4.73 \times 10^{-3}$ GPa^{-1} at room T. However, they estimated a decrease in κ of ∼7% between 298 and 4 K. Thus, the estimated low T value of κ is $\sim 4.40 \times 10^{-3}$ GPa^{-1}, only ∼4% larger than the calculated value.

The calculated pressure dependence of the parameter u, which locates the oxygen atoms within the unit cell, is well fitted by a straight line. As shown in figure 2, the experimental error bars for the measured values of u are such that a precise quantitative comparison is meaningless. However, at all pressures, the calculated values are close to the range of values covered by the experimental error bars.

It is worth noting that a decreases approximately three times faster than c as P rises. As it was postulated before [38], this may be due to metal–metal repulsion parallel to c across the shared octahedral edge. As a consequence, the c/a ratio increases with pressure, in agreement with experimental observations [37, 38].

Table 1 also shows the coefficients of the linear fit for the two closest Ti–O contacts. As seen experimentally [37], the longest Ti–O distance shrinks faster than the shortest

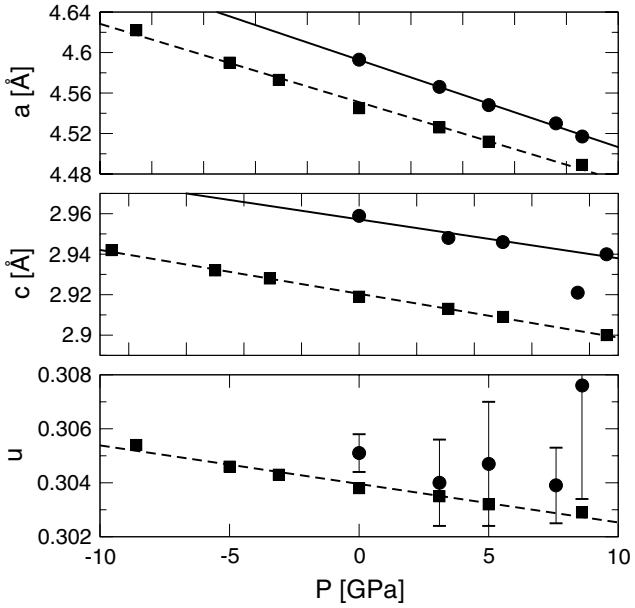

Figure 2. The variation of the equilibrium structural parameters a, c and u with pressure P. Squares and circle correspond to the calculated and measured values, respectively. The linear term of the calculated and measured pressure dependence is represented with dashed and solid lines, respectively. The experimental error bars are shown for the parameter u only as they lie within the size of the circles for the other parameters.

distance. Also, the difference between the two distances is reduced as the pressure increases. Experimentally, this trend is reversed at ∼8 GPa and a linear extrapolation from the present calculations suggests that, at $T = 0$, the trend inversion occurs at ∼9 GPa.

Muscat *et al* [25] performed analogous calculations within the Hartree–Fock approximation. In agreement with our findings, all structural parameters vary linearly with pressure. In these previous calculations, a and c systematically underestimate and overestimate, respectively, the measured values and therefore lead to values of Ω in closer agreement with experiment.

3.2. The variation of the structure with uniaxial strain

To investigate the effects of a uniaxial strain along the c-axis upon the structure of bulk rutile, the lattice parameter c is constrained to have values 2, 4 and 6% larger than the equilibrium value at zero pressure. For each of these enlarged values of c the lattice parameters in the a–b plane as well as all internal atomic coordinates are optimized. Figure 3(a) reports the variation of the lattice constant a ($a = b$ as the structure is tetragonal) as a function of c. As expected, a decreases as c increases, because of the tendency of the system to preserve the unit cell volume, Ω. The decrease in a, however, is insufficient to preserve the volume, which increases slightly, as illustrated in figure 3(b). For instance, when c is strained by ∼3% the volume increases by roughly 1%. Figure 3(c) shows that the parameter u, which determines the fractional coordinates of the oxygen atoms, increases only very marginally with c. Figure 3 also shows that, as in the case reported in the previous section, the structural parameters vary linearly with the strain over the range considered.

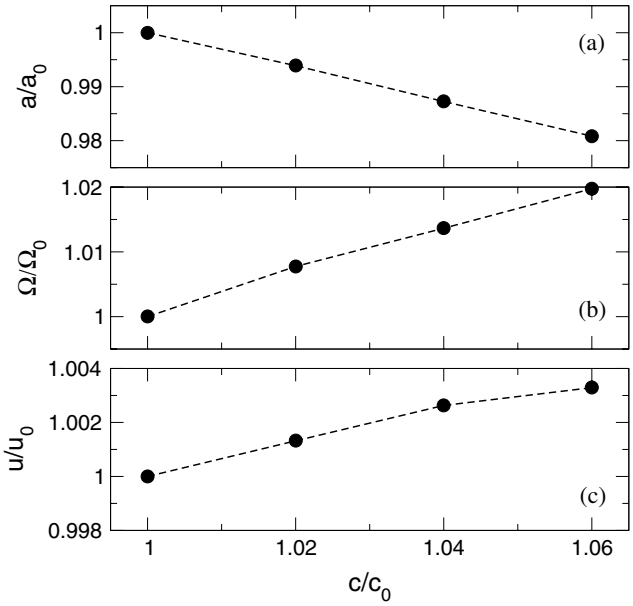

Figure 3. Relative variation of the structural parameters as a function of the uniaxial strain along the *c*-axis. In all cases the subscript '0' refers to the value at zero pressure and zero strain. a is the lattice constant in the a–b plane, Ω is the unit cell volume and u locates the oxygen atoms within the unit cell.

3.3. Vibrational frequencies versus pressure

Starting from the optimized geometries at each pressure, the Γ-point vibrational harmonic frequencies and eigenvectors are calculated. As explained in a recent report [15], the present calculations do not include the long-range electrostatic fields that cause the frequencies of the longitudinal optic (LO) modes to split from their transverse (TO) counterparts in the long-wavelength limit. Therefore only the frequencies of the TO phonons are reported here. The close agreement between the calculated frequencies at zero pressure and the experimental values [2, 39, 40] and other LDA calculations [14] has been demonstrated previously [15]. It was found that the calculated frequencies are in excellent agreement with the measured frequencies, especially if compared with the low-temperature ($T \sim 4$ K) data[1]. The deviation from experiment is $\sim$13 cm^{-1} at most and is often much smaller than that. For instance, the deviation drops to no more than $\sim$2 cm^{-1} for the two stiffest modes, B_{2g} and A_{1g}, and remains small also for several of the softer modes. It is known, however, that the softer modes are more affected by numerical inaccuracy and carry the largest error bars. The atomic displacements associated with the modes that will be discussed in detail below, i.e. the A_{2u}, softest E_u and B_{1g} modes, are shown in figure 1. Despite the soft nature of these modes, there is good agreement with experiment. The calculated frequency for the A_{2u} mode is 154.4 cm^{-1} and the low-temperature measurements give 142 cm^{-1} [2] and 144 cm^{-1} [39, 40]. The present work predicts the softest E_u mode to have a frequency of 191.4 cm^{-1} which compares well with the measured values of 189 cm^{-1} [2] and 183 cm^{-1} [39, 40]. To the best of the authors' knowledge, low-temperature experimental data for this frequency have not

[1] The present calculations do not include the effects of temperature and therefore the calculated properties correspond to the zero-temperature case.

Table 2. Calculated frequencies, logarithmic pressure derivatives and mode Grüneisen parameters, γ, of the Γ-point phonons. The available measured mode Grüneisen parameters [3] are reported in brackets.

Modes	$\omega(P=0)$ (cm^{-1})	$\left(\frac{\partial \ln \omega}{\partial P}\right)_T$ (10^{-2} GPa^{-1})	γ
B_{2g}	824.7	0.63	1.49
A_{1g}	611.6	0.74	1.76 (1.59)
E_u (TO)	488.4	0.40	0.95
E_g	463.2	0.69	1.64 (2.43)
A_{2g}	421.7	0.17	0.40
B_{1u}^2	393.0	1.12	2.66
E_u (TO)	383.9	0.99	2.35
B_{1g}	137.0	−2.62	−6.21 (−5.03)
B_{1u}[a]	104.0	1.73	4.10
E_u (TO)[a]	191.4	3.89	9.21
A_{2u} (TO)[a]	154.4	5.80	13.74 (13.32)

[a] $\ln \omega$ does not vary linearly with P for negative values of P. Thus, the logarithmic pressure derivative and the Grüneisen parameter of these modes are obtained from the data at non-negative pressure only.

been reported so far. The B_{1g} computed frequency is 137.0 cm^{-1} which compares well with the measurements (142 cm^{-1} [2] and 143 cm^{-1} [39, 40]). For these specific frequencies the comparison with previous similar calculations [14] is less satisfactory. Lee *et al* [14] obtained 176.1 and 164.8 cm^{-1} for the A_{2u} and E_u modes, respectively, and 125.2 cm^{-1} for the B_{1g} mode. These discrepancies probably arise from the slight differences in the equilibrium lattice constants predicted by the calculations. The zero-pressure equilibrium lattice parameters predicted by these calculations are $a = 4.545$ Å and $c = 2.919$ Å. The values found by Lee *et al* [14] are $a = 4.536$ Å and $c = 2.915$ Å. Although these structural parameters differ only by a fraction of a per cent, this difference is amplified in the calculation of these frequencies due to their extreme sensitivity to the lattice parameters. Therefore, small differences in the parameters can lead to sizeable differences. For example, the ordering of the A_{2u} and E_u frequencies is opposite in the two calculations. Although the present calculations reproduce the measured ordering, due to the sensitivity of the properties investigated in this work the quantitative information provided here should be considered as an estimate of the true values. Figure 4 illustrates the pressure dependence of the calculated frequencies. In table 2 the zero-pressure frequencies, ω, are reported together with their logarithmic pressure derivatives and the mode Grüneisen parameters $\gamma = (-\frac{\partial \ln \omega}{\partial \ln \Omega})_T = \frac{1}{\kappa}(\frac{\partial \ln \omega}{\partial P})_T$. The values of γ were derived from the latter expression, where the value of the volume compressibility, κ, is obtained by the present calculations as described in section 3.1. Overall, the calculated mode Grüneisen parameters agree well with the available measured values [3], reported in brackets in table 2. A more detailed comparison with experiment will be done for the specific modes analysed in the following sections.

3.4. Softening of the c-axis ferroelectric mode as a function of isotropic pressure

The TO A_{2u} mode, the only polar mode in rutile along the c-axis, displays the largest Grüneisen parameter of all modes investigated here. As shown in figure 1(a), this mode involves a rigid displacement of the Ti sublattice along the c-axis and an analogous displacement of the O sublattice but with opposite sign. Samara and Peercy [3] measured the pressure dependence of the c-axis dielectric constant, ϵ_c, over the range 0–4 kbar at several temperatures, and used

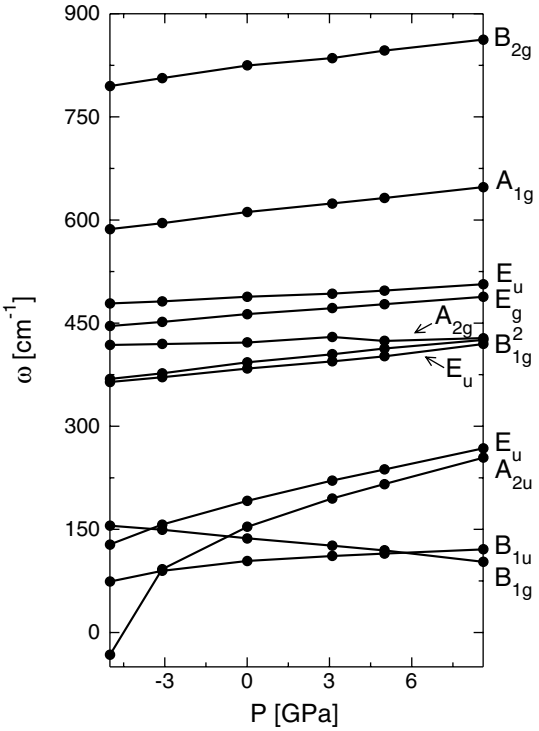

Figure 4. Pressure dependence of the Γ-point vibrational frequencies of TiO_2 rutile. The labelling of the modes follows [2], where the eigenvectors relative to each mode are also shown. The lines only provide a guide for the eye.

these data to derive the pressure dependence for the TO A_{2u} frequency. They found a value of $(5.9 \pm 0.15) \times 10^{-2}$ GPa^{-1} for the logarithmic pressure derivative of its frequency. Our data extend over a much wider range and a linear fit to the non-negative pressure values gives a value of 5.8×10^{-2} GPa^{-1}, in excellent agreement with this measurement. The computed Grüneisen parameter, γ, of this mode is 13.74, in excellent agreement with the low T experimental γ, equal to 13.32 [3].

The variation of the total energy with the lattice distortion along the mode is displayed in figure 5 for three values of pressure ($P = -8.6, 0$ and +8.6 GPa). As the pressure decreases, the positive curvature around the equilibrium atomic positions at zero pressure quickly decreases and eventually becomes negative. The frozen phonon approach [41] can be used to extract the harmonic frequency from these energy profiles. The result is shown in figure 6. The frequency decreases with pressure, vanishes at ~ -4 GPa and is imaginary below this pressure. Therefore, the present calculations predict that, at $P \sim -4$ GPa, rutile becomes unstable with respect to a distortion along the eigenvector of this mode. Because this is the ferroelectric mode along the *c*-axis, this result implies that bulk TiO_2 rutile is *near* a ferroelectric phase transition that can be triggered by applying negative isotropic pressure to the crystal. Figure 4 shows that for values of pressure below the transition pressure the minimum energy geometry is one where the (normally coincident) Ti and O planes perpendicular to the *c*-axis are slightly separated. At $P = -8.6$ GPa this separation is ~ 0.06 Å.

TiO_2 rutile has a positive thermal expansion coefficient, i.e. its volume expands as T increases. However, as T increases the frequency of this mode *increases* rather than

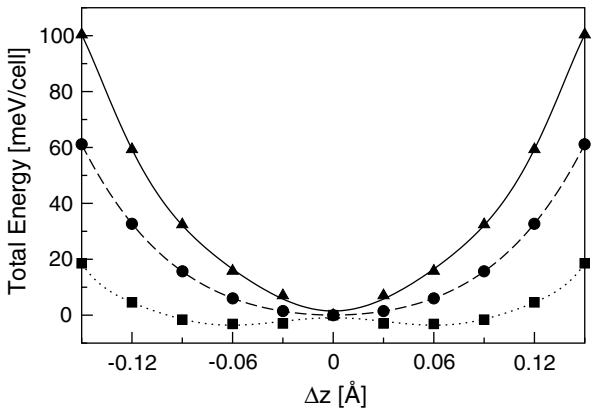

Figure 5. Total energy variation per unit cell as a function of the atomic displacements along the A_{2u} vibrational mode. Δz labels the variation in the z-component of the Ti–O distances. The curves only provide a guide for the eye. Squares and the dotted curve correspond to $P = -8.6$ GPa, circles and the dashed curve to $P = 0$; the data at $P = +8.6$ GPa are represented as triangles and the solid curve. For each value of pressure, the origin of the energy axis coincides with the total energy of the undistorted structure at that pressure.

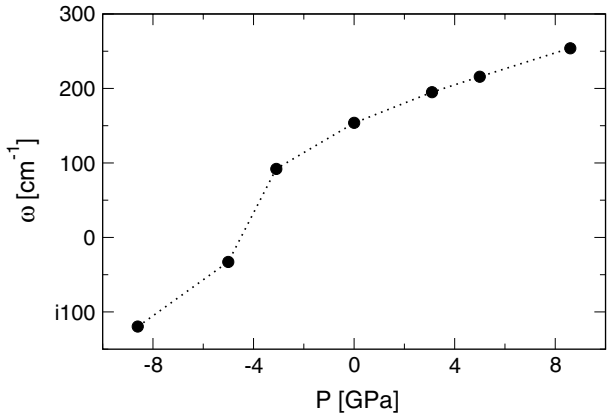

Figure 6. Harmonic frequency of the A_{2u} vibrational mode as a function of pressure. The curve only provides a guide for the eye.

decreases. Samara and Peercy [3] have explained this apparent paradox by separating the overall temperature effect into a pure-volume and a pure-temperature contribution. As T is increased, the pure-volume effect tends to lower the frequency, whereas the pure-temperature effect, which dominates, increases the frequency. The present work provides a rationale for this behaviour, which will be illustrated in section 3.6.

Because of the sharp increase in the dielectric constant as the ferroelectric transition is approached, we estimate that if TiO_2 rutile can be produced with a cell volume $\sim$2% larger than its equilibrium value at low T, one would obtain a material with highly enhanced dielectric properties. Unfortunately, because of the pure-temperature effect on the phonon frequency, this cannot be achieved through thermal expansion. 'Chemical' mechanisms for lattice expansion may be possible through, for instance, the insertion of larger atoms as substitutional defects that would not affect the electronic and chemical properties of the system or atom intercalation

into the lattice [42]. It is also possible that the largely enhanced dielectric properties of nanostructured rutile-phase titania measured by Ye *et al* [43] are related to the volume effects predicted here.

As mentioned in section 1, the possibility of inducing a ferroelectric phase transition by applying negative isotropic pressure was found for other incipient ferroelectric materials, namely $KTaO_3$ [4] and $CaTiO_3$ [5]. Both these systems, however, have the perovskite structure and this is the first report of such an effect occurring for the rutile structure. An interesting question arises as to whether the microscopic mechanisms at the origin of the ferroelectric stabilization in these two different structures have similarities. This question will be addressed in section 3.6.

The second largest mode Grüneisen parameter in table 2 refers to the softest TO E_u mode, which is the analogue of the A_{2u} mode in the *a*–*b* plane (see figure 1(b)). This mode also softens as the pressure diminishes and eventually becomes imaginary. A third-order polynomial fits well the obtained data for the pressure dependence of this frequency and can be used to extrapolate the results to zero-frequency in order to estimate the predicted transition pressure. This procedure yields a critical pressure of about -15 GPa. In summary, a much larger negative pressure would be needed to trigger an instability along this mode compared to the analogous mode along the *c*-axis and it is unlikely that the rutile phase is stable up to such very large values of negative pressure.

3.5. Softening of the c-axis ferroelectric mode as a function of uniaxial strain

A ferroelectric phase transition brought about by the softening of the *c*-axis ferroelectric mode can also be induced by uniaxial strain along the same axis. This is illustrated in figure 7, which reports the shape of the energy profile for a lattice distortion along the A_{2u} mode for several values of the uniaxial strain. These profiles can be used to extract the frequency of the mode as a function of the strain. The outcome, reported in figure 8, shows that the frequency decreases, vanishes when the strain in *c* is just over 3% and then becomes imaginary. Thus, the present calculations predict that rutile will undergo a ferroelectric phase transition if *c* is increased by just over 3%.

As the A_{2u} mode is the only ferroelectric mode along the *c*-axis, the Lyddane–Sachs–Teller relation [44] for the *c*-axis reduces to:

$$\frac{\epsilon_c}{\epsilon_{\infty,c}} = \left(\frac{\omega_{f,\mathrm{LO}}}{\omega_{f,\mathrm{TO}}}\right)^2, \tag{2}$$

where ω_f denotes the frequency of the TO A_{2u} mode. This equation could be used to extract the volume dependence of ϵ_c if the volume dependence of all the other quantities in the equation were known. Lee *et al* [14] showed that the LO–TO splitting in TiO_2 rutile at zero pressure is enormous, with $\omega_{f,\mathrm{LO}} = 769.3\ \mathrm{cm}^{-1}$, nearly 600 cm^{-1} higher than its TO counterpart. The TO mode corresponds to zero electric field and, therefore, the restoring forces acting on the vibrating atoms are mostly due to the local atomic environment. In addition to these forces, the atoms vibrating in the LO mode are subjected to a force due to the long-range electric field. The LO frequency is much larger than the TO frequency and this suggests that the forces generated by the electric field dominate in the determination of the LO frequency. Based on this argument, it is generally expected that the pressure dependence of the TO mode is stronger than that of the LO mode because the pressure affects the local environment. Therefore, just for the purpose of gaining an indication of the pressure dependence of ϵ_c as the phase transition is approached, the pressure dependence of ϵ_∞ and $\omega_{f,\mathrm{LO}}$ can be neglected because the main contribution to the change in ϵ_c will be due to $\omega_{f,\mathrm{TO}}$ approaching zero. Under this

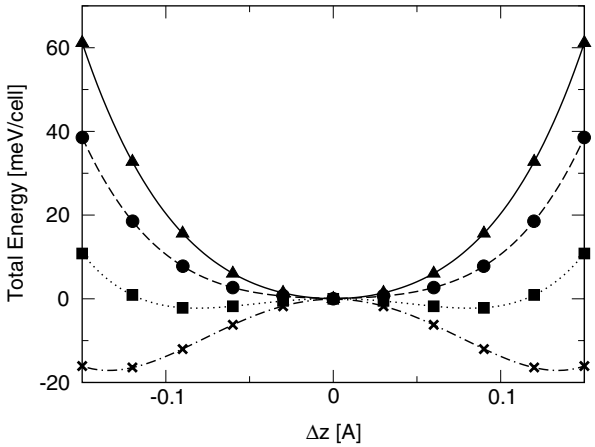

Figure 7. Total energy variation per unit cell as a function of the atomic displacements along the A_{2u} vibrational mode. Δz labels the variation in the z-component of the Ti–O distances. The curves only provide a guide for the eye. Triangles and the solid curve correspond to zero uniaxial strain along the c-axis, circles and the dashed curve to a 2% strain; the data at 4% strain are represented as squares and dotted curve. Crosses and the dash–dotted curve refer to a 6% strain. For each value of the strain, the origin of the energy axis coincides with the total energy of the undistorted structure at that strain.

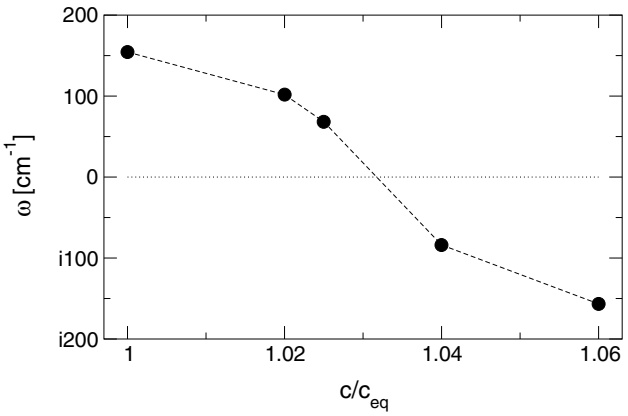

Figure 8. Harmonic frequency of the A_{2u} vibrational mode as a function of uniaxial strain along the c-axis. The curve only provides a guide for the eye.

approximation the pressure-dependent part of equation (2) reduces to:

$$\epsilon_c = \frac{\text{const}}{\omega^2_{f,\text{TO}}}. \tag{3}$$

An estimate of the value of the constant is provided by the measured ambient-condition values of $\epsilon_c = 166.2$ and $\omega_{f,\text{TO}} = 172\ \text{cm}^{-1}$ [3]. Figure 9 shows the dramatic increase in the c-axis dielectric constant on the approach of the ferroelectric phase transition caused by the uniaxial strain. The present calculations predict this dielectric constant to double when c is increased by 2% (corresponding to an decrease by 0.7% in a, as shown in figure 3(a)) and to become larger than 1000 for a 2.5% increase in c. It is important to remark that this critical strain is brought about by a decrease of just 1% in the lattice constants in the a–b plane. This

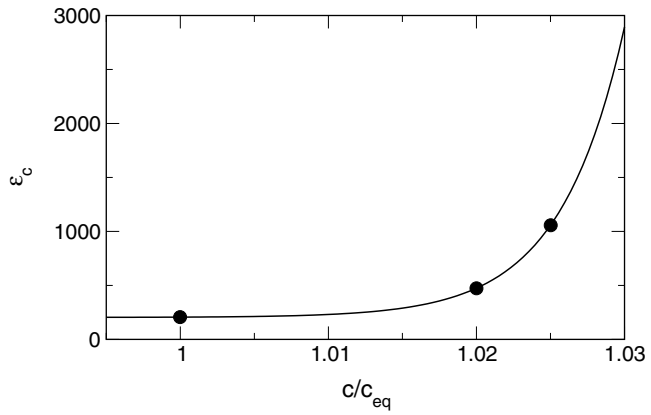

Figure 9. *c*-axis dielectric constant as a function of the uniaxial strain along the same axis. The curve only provides a guide for the eye.

modification of the cell parameters might be induced by epitaxially growing a thin film of TiO_2 rutile on a substrate with a small lattice mismatch. In this way thin films with significantly enhanced dielectric properties might be produced. To the authors' knowledge, the possibility of inducing a ferroelectric transition by applying uniaxial strain has not been previously reported.

One can now speculate that if a strain were applied to enlarge the lattice constants in the *a*–*b* plane, the frequency of the softest TO E_u mode, which is the analogue of the A_{2u} mode in the *a*–*b* plane, would also soften and eventually lead to a ferroelectric instability in the *a*–*b*-plane. However, because the zero-pressure value of the frequency of this mode is higher than that of the A_{2u} mode and the Grüneisen parameter is lower, it is reasonable to expect that the critical value of the strain for stabilizing an in-plane ferroelectric distortion would be higher than in the *c*-axis case. In addition, because this E_u mode is not the only ferroelectric mode in the *a*–*b* plane (whereas the A_{2u} mode is the only ferroelectric mode along the *c*-axis) the influence of this mode's softening on the dielectric constants is less obvious.

3.6. Origin of the ferroelectric stabilization

In order to understand the origin of the ferroelectric stabilization of TiO_2 rutile, further calculations have been performed to analyse the contributions to the total energy for the system with a *c*-axis strain of 6%. An analogous analysis of the case in which the ferroelectric stabilization is achieved through an isotropic expansion of the cell leads to the same qualitative conclusions and therefore will not be presented. Figure 7 shows that, for a 6% strain, the paraelectric geometry, i.e. where the Ti atom is at the centre of the O octahedron, is unstable with respect to the ferroelectric geometry where the z-component of the Ti–O distance, Δz, is equal to 0.12 Å.

The stability of the paraelectric and ferroelectric structures can be investigated by using a simple ionic model. In this model, the Ti and O atoms are described as formally charged ions (i.e. Ti^{4+} and O^{2-}) and the short-range repulsion is represented by a Buckingham-type potential [45]. When the ferroelectric distortion is applied, the Madelung energy decreases by 0.727 eV whereas the short-range repulsive interaction increases by 1.011 eV. Therefore, it is clear that in this simple model the short-range repulsive forces favour the paraelectric geometry, whereas the long-range electrostatic interactions favour the ferroelectric geometry. For the applied strain, the short-range forces prevail and the paraelectric phase is more stable

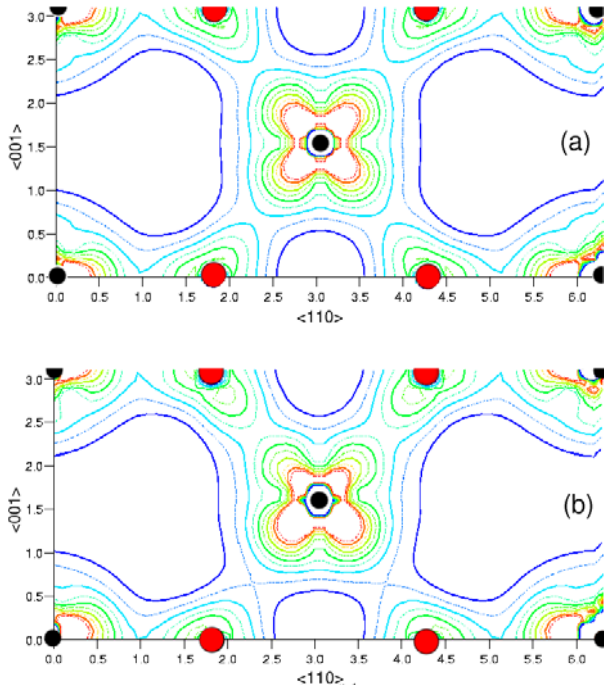

Figure 10. Difference between the self-consistent total electron charge density and the one obtained by overlapping spherical Ti^{4+} and O^{2-} ions. A 6% strain along the *c*-axis is applied. The smaller circles represent the Ti atoms and the larger circles represent the O atoms. The plane shown is the plane through the Ti–O bonds parallel to the *c*-axis. Panels (a) and (b) refer to the paraelectric and ferroelectric geometries, respectively. The charge-density contour-lines range from 0 to 0.07 e $Å^{-1}$ and are separated by a 0.008 e $Å^{-1}$ interval.

(This figure is in colour only in the electronic version)

by 0.284 eV. However, one can imagine that if the lattice is expanded further, the short-range repulsive forces would decrease and eventually the ferroelectric phase would become the most stable. This is evidenced by the fact that also in this model the frequency of the TO A_{2u} mode softens as the lattice is expanded.

This simple ionic model allows the effects of the short-range repulsion forces and long-range electrostatic interactions to be separated but does not agree qualitatively with the DFT calculations because it neglects the effects of covalency and electronic charge polarization. The important role of these effects, however, is apparent when further analysis of the DFT data is carried out. The difference between the self-consistent electron charge density and the charge density obtained as an overlap of the spherical, formally charged ions highlights the presence of these effects. Figure 10 shows two-dimensional plots of this electron charge density difference for the unstable paraelectric (a) and stable ferroelectric (b) geometries. Both panels (a) and (b) show a significant degree of polarization of the Ti ions. This evidence defies the general view according to which charge polarization effects in oxides are largely dominated by the dipolar polarization of the O ions. From the shape of the charge density isosurfaces around the Ti ion, it is apparent that in the ferroelectric geometry a significant further polarization is added to the polarization that exists in the paraelectric phase.

The Mulliken population analysis of the LCAO results shows that the ionicity of the system, even at the zero-pressure and unstrained equilibrium geometry, is much lower than that of the

formally charged ionic model. Moreover, the ferroelectric distortion causes a further slight decrease in the ionicity of the system and the charge on the Ti atom is reduced from +2.08 to +2.06. More specifically, the orbital population data show that the O 2p orbital donates electron charge to the Ti 3d orbitals (mainly the d_{xz} and d_{yz} orbitals). Thus, the ferroelectric distortion induces a back-donation of electrons from the oxygen to the titanium ions. This indicates an increase in the degree of hybridization between the orbitals involved in this process. It is this enhanced hybridization that reduces the short-range repulsion and therefore stabilizes the ferroelectric phase. This effect has been observed by several authors in perovskite oxides such as $BaTiO_3$ [6, 7], $PbTiO_3$ [7], $KTaO_3$ [8], $SrBi_2Ta_2O_9$ [9] and $CaTiO_3$ [5]. Cohen and co-workers [6, 7], in particular, illustrated how this hybridization is essential to the stabilization of the ferroelectric phase in $BaTiO_3$ and $PbTiO_3$. Their linearized augmented plane-wave calculations showed that if 'the Ti d energy parameter is raised up above the 4d asymptote, effectively removing the Ti 3d states from the variational basis, the ferroelectric state is lost and the formerly unstable mode becomes a high-frequency mode'. A similar result is generated from the present LCAO calculations when the lowest Ti d-orbital is removed from the basis set. Cohen and co-workers concluded that for ferroelectric perovskites of type ABO_3 in general, 'hybridization between the B cation and O is essential to weaken the short-range repulsion and allow the ferroelectric transition'. We can now widen the significance of this conclusion by adding that this effect is not typical of perovskites only, but also occurs in rutile. What links these structures is the existence of an O octahedron occupied by a cation whose lowest unoccupied states are d-states and where the level of ionicity is significantly lower than the formal ionicity.

The charge redistribution induced by the ferroelectric distortion is very slight and is therefore consistent with the small energy difference ($\sim$20 meV) between the paraelectric and the ferroelectric phases predicted by the calculations for a 6% strain along the *c*-axis. The subtlety of these effects evidences the existence of a very delicate balance between the short-range forces and the long-range electrostatic interactions. At zero pressure and zero strain this balance only very slightly favours the paraelectric phase. The high dielectric constants and the incipient ferroelectricity of rutile flag the vicinity of an inversion in this balance, i.e. of a ferroelectric phase transition. The application of a negative isotropic pressure or of a uniaxial strain lowers the short-range repulsion and therefore tips the balance in favour of the ferroelectric phase.

Incidentally, this result also explains why thermal expansion counter-intuitively causes a hardening of the TO A_{2u} mode. As mentioned in section 3.4, Samara and Peercy [3] separated the pure-volume contribution of the thermal expansion from the pure-temperature contribution. The pure-volume contribution causes a softening of this mode, in agreement with the present work. However, the pure-temperature contribution, which dominates in this instance, causes a hardening of the mode. In the light of what has just been described, the reason for this temperature effect becomes clear. A temperature increase causes an increase in the effective short-range interatomic repulsion and reduces the influence of the long-range electrostatic interactions.

3.7. B_{1g} mode versus isotropic pressure and the rutile to $CaCl_2$-type transition

The Grüneisen parameter γ for the B_{1g} mode (shown in figure 1(c)), is negative, meaning that the mode frequency unusually decreases as the pressure increases. The calculated logarithmic pressure derivative and relative γ agree well with the measured values of $(-2.38 \pm 0.2) \times 10^{-2}$ GPa^{-1} [3, 22] and -5.03 [3], respectively. As described in section 1, this negative Grüneisen parameter led us to speculate about the existence of a phase transition

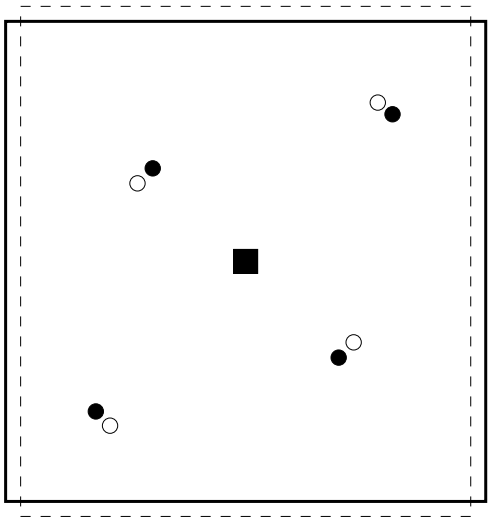

Figure 11. Unit cells of rutile and $CaCl_2$-type structures projected on the (001) plane. The small filled circles represent the positions of the O atoms in the unit cell of rutile (solid line). The empty circles represent the positions of the O atoms in the unit cell of the $CaCl_2$-type structure (dashed line). The filled square represents the position of the central Ti atom in both structures.

which may be induced by this mode softening. As shown in figure 11, an atomic displacement along the B_{1g} mode transforms rutile into a $CaCl_2$-type structure, when accompanied by an orthorhombic deformation of the unit cell. This observation is supported by the evidence [26–28] that this is the mechanism for the transition from stishovite (the rutile-structured SiO_2) to the $CaCl_2$-type structure, which occurs at about 50 GPa. In order to establish the feasibility of such a phase transformation, the pressure dependence of the shear modulus, $c_{11} - c_{12}$, is investigated here. Starting from the equilibrium geometry of rutile at each pressure, the unit cell is slightly deformed under an orthorhombic strain and the atomic positions within the cell are reoptimized. This procedure allows for the coupling between the unit cell distortion and a distortion of the atomic positions along the B_{1g} mode. The result is reported in figure 12. The zero-pressure value of the shear modulus predicted by the present calculations is 95.7 GPa, in excellent agreement with the experimental value of 93 GPa [46]. As the pressure increases, the shear modulus decreases, vanishes at about 13 GPa and becomes negative. This indicates the occurrence of an instability in favour of the orthorhombic $CaCl_2$-type structure. The instability will lead to an actual phase transition if rutile can exist as such up to this critical pressure. This result is confirmed by performing full geometry optimizations starting from orthorhombically strained unit cells of rutile at pressures between 10 and 20 GPa. Below 13 GPa the system recovers the tetragonal rutile structure and there is a continuous and smooth change to an orthorhombic structure as the pressure increases above 13 GPa. Figure 13 illustrates this point by showing the unit cell volume as a function of pressure for the two phases of rutile and $CaCl_2$. A similar smooth behaviour across the transition pressure is observed for the lattice parameters a, b and c and for the positions of the oxygen atoms within the cell. Further evidence for the continuous, i.e. second-order, nature of the transition is shown in figure 14, which illustrates the smooth change in the total energy per cell across the transition pressure. The analogous transition of stishovite, the rutile-structured SiO_2, occurs at about 50 GPa. Density functional calculations [28] similar to the present study have predicted the transition to be of second order and to occur at around 47 GPa, in excellent agreement with experiment.

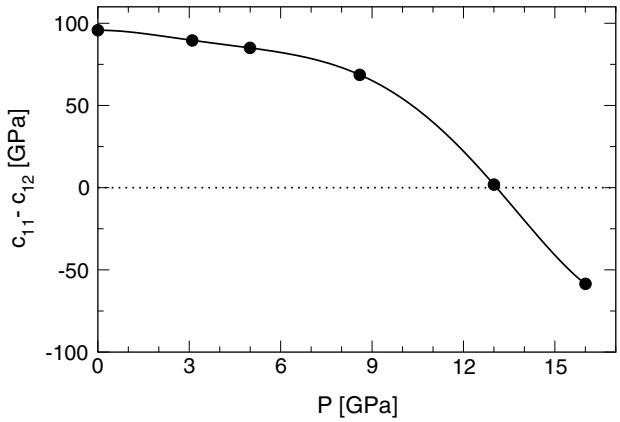

Figure 12. Calculated pressure dependence of the shear modulus, $c_{11} - c_{12}$, of TiO_2 rutile.

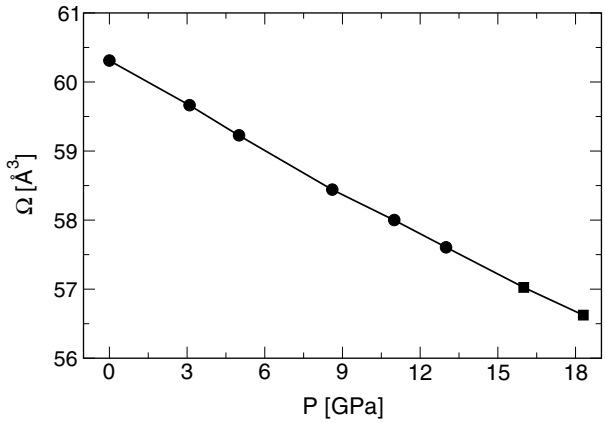

Figure 13. Pressure dependence of the unit cell volumes of rutile (circles) and $CaCl_2$ (squares) type structures.

At present, there is no experimental evidence of the existence of a $CaCl_2$-type structure for TiO_2. It may be that the rutile to columbite transformation occurs at values of pressure just below the critical pressure for the rutile to $CaCl_2$ transition and thus precludes the observation of the latter transition. However, the critical pressure for this transition predicted here is close to the range of pressure (5–12 GPa) over which the sluggish rutile to columbite transition is observed. Furthermore, the second-order nature of the rutile to $CaCl_2$ transition causes only subtle structural changes which may be difficult to detect experimentally. Therefore, it is not possible at present to establish conclusively the existence of a transition to the $CaCl_2$-type structure in TiO_2. Detailed structural measurements for well equilibrated samples in the pressure range 5–12 GPa would be of great interest.

The extrapolation to zero frequency obtained from the present calculations shows that the B_{1g} frequency does not vanish at the predicted value for the rutile to $CaCl_2$ transition pressure. However, this observation is not in conflict with the second-order nature of the transition, as was argued by Samara and Peercy [3]. As discussed in detail by Karki *et al* [28] for the case of SiO_2, although the transition is of second order, the B_{1g} mode does not soften completely at the

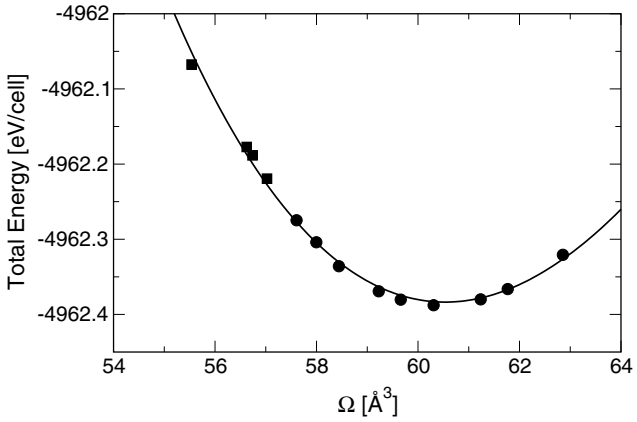

Figure 14. Total energy per cell as a function of the unit cell volume for rutile (circles) and the $CaCl_2$-type structure (squares).

transition point if an orthorhombic distortion of the cell is not allowed to happen simultaneously with atomic displacements along the vibrational mode.

The present calculations also help in gaining insight into the mechanism for the softening of the B_{1g} mode induced by the increasing pressure if the contributions to the rise in the total energy as the atoms are displaced along the mode are analysed. As the pressure increases, it is the contribution of the electronic kinetic energy which decreases significantly and causes the mode softening. The reason for this lies in the structural changes induced by the distortion. Indeed, as the atoms are displaced along this mode, the Ti–O bond distances increase and so do the closest O–O contacts. It is therefore reasonable to conclude that the softening occurs because a displacement along the mode partially relieves the bond compression caused by the pressure increase. The main effect of the relief of the bond compression is the decrease in the kinetic energy of the valence electrons.

The remaining modes listed in table 2 have rather small Grüneisen parameters and it is therefore unlikely that they may cause a pressure-induced transition. Experimental data for their pressure dependence are available only for the Raman modes and at room T. It is noticed that the calculated Grüneisen parameter for the A_{1g} mode agrees very well with the experimental value of 1.59 [3], but the agreement is significantly worse for the doubly degenerate E_g mode, for which the measured value equals 2.43. Otherwise, the agreement between the measured and calculated quantities in table 2 is good. It should be noted that this is the first time that the pressure dependence of several of the Γ-point modes of TiO_2 rutile has been investigated.

All of the results discussed here were obtained within the plane-wave pseudopotential implementation of DFT described in section 2. Calculations were repeated with the all-electron LCAO scheme discussed in section 2. Apart from very slight quantitative differences, in all cases the all-electron calculations agree well with the plane-wave, pseudopotential results, thus confirming their independence of the particular numerical scheme used to implement DFT. In particular, this confirms that the current results are not a spurious effect of the pseudopotentials used.

4. Summary and concluding remarks

This paper presented density functional calculations of the geometry and Γ-point phonons of TiO_2 rutile over a range of hydrostatic pressures and c-axis uniaxial strains.

The logarithmic pressure derivative of the frequencies with respect to the hydrostatic pressure and the mode Grüneisen parameters were found to agree well with the available experimental data.

The *c*-axis TO ferroelectric mode A_{2u} decreases quickly as the hydrostatic pressure decreases, vanishes at ~ -4 GPa and becomes imaginary, thereby leading to a crystal instability with respect to a distortion of the crystal along this mode. Thus, rutile is found to be *near* a ferroelectric phase transition that can be induced by applying negative hydrostatic pressure.

A similar transition occurs when the *c*-axis is strained by just over 3%. To the best of the authors' knowledge, the possibility of inducing a ferroelectric phase transition in an incipient ferroelectric by applying anisotropic strain has not been previously reported. Because of the dramatic increase in the static dielectric constants on the approach of a ferroelectric phase transition, this result suggests the possibility of designing a TiO_2 rutile-based material with enhanced dielectric properties. Such structures might be synthesized via thin film growth on a substrate with a small lattice mismatch. The present calculations suggest that a reduction by 0.8% in the lattice parameters in the *a*–*b* plane is sufficient to produce a ten-fold increase in the *c*-axis dielectric constant.

The vicinity of the ferroelectric instability in TiO_2 rutile is due to a very delicate balance between short-range repulsive forces, which favour the paraelectric phase, and long-range electrostatic forces, which favour the ferroelectric phase. The application of negative hydrostatic pressure or uniaxial strain lowers the short-range repulsion, thereby leading to the softening of this mode and eventually to the ferroelectric phase transition. It was found that an increase in the hybridization between the Ti 3d and the O 2p orbitals is essential for the stabilization of the ferroelectric phase. Previous studies had established that the same mechanism stabilizes the ferroelectric phase in perovskite oxides. The present work now extends the conclusions drawn about the origin of the ferroelectric stabilization in perovskites to include a material based on the rutile structure.

In addition, the pressure-induced softening of the B_{1g} mode and the corresponding phase transformation to a $CaCl_2$-type structure was investigated with the aim of quantifying the critical pressure for the transition and analysing the atomistic origin of the softening. It was found that the transition would occur at a pressure of $\sim$13 GPa if rutile could exist as such up to the critical pressure. The crystal distortion along this mode relieves the Ti–O and closest O–O bond compression caused by the increased pressure, thereby flattening the kinetic energy profile along the mode as the pressure increases.

Acknowledgments

The support of the EPSRC is gratefully acknowledged both for BM under the UKCP consortium Grant (GR/N02337/01) and for the provision of a cluster of 32 dual-processor PCs, located at Daresbury Laboratory, on which some of the calculations were performed. Other calculations were performed on the CRAY T3E at the EPSRC's, CSAR service, Manchester.

References

[1] Parker R A 1961 *Phys. Rev.* **124** 1719
[2] Traylor J G, Smith H G, Nicklow R M and Wilkinson M K 1971 *Phys. Rev.* B **3** 3457
[3] Samara G A and Peercy P S 1973 *Phys. Rev.* B **7** 1131
[4] Postnikov A V, Neumann T, Borstel G and Methfessel M 1993 *Phys. Rev.* B **48** 5910
[5] Wang Y X, Su X T and Zhong W L 2002 *Chin. J. Chem. Phys.* **15** 29
[6] Cohen R E and Krakauer H 1990 *Phys. Rev.* B **42** 6416
[7] Cohen R E 1992 *Nature* **358** 136

[8] Singh D J 1996 *Phys. Rev.* B **53** 176
[9] Stachiotti M G, Rodriguez C O, Ambrisch-Draxl C and Christensen N E 2000 *Phys. Rev.* B **61** 14434
[10] Dubrovinsky L S, Dubrovinskaia N A, Swamy V, Muscat J, Harrison N M, Ahuja R, Holm B and Johansson B 2001 *Nature* **410** 653
[11] Gervais F and Kress W 1983 *Phys. Rev.* B **28** 2962
[12] For a review of investigations based on empirical models see Swamy V, Gale J D and Dubrovinsky L S 2001 *J. Phys. Chem. Solids* **62** 887
[13] Swamy V, Muscat J, Gale J D and Harrison N M 2002 *Surf. Sci.* **504** 115
[14] Lee C, Ghosez Ph and Gonze X 1994 *Phys. Rev.* B **50** 13379
[15] Montanari B and Harrison N M 2002 *Chem. Phys. Lett.* **364** 528
[16] Perdew J P 1991 *Electronic Structure of Solids '91* ed P Ziesche and H Eschrig (Berlin: Akademie) p 11
[17] Perdew J P, Burke K and Ernzerhof M 1996 *Phys. Rev. Lett.* **77** 3865
[18] Nagel L and O'Keeffe M 1971 *Mater. Res. Bull.* **6** 1317
[19] Nicol M and Fong M Y 1971 *J. Chem. Phys.* **54** 3167
[20] Merle P, Pascual J, Camassel J and Mathieu H 1980 *Phys. Rev.* B **21** 1617
[21] Mammone J F, Sharma S K and Nicol M 1980 *Solid State Commun.* **34** 799
[22] Mammone J F, Nicol M and Sharma S K 1981 *J. Phys. Chem. Solids* **42** 379
[23] Arashi H 1992 *J. Phys. Chem. Solids* **53** 355
[24] Liu L-G and Mernagh T P 1992 *Eur. J. Mineral.* **4** 45
[25] Muscat J, Swamy V and Harrison N M 2002 *Phys. Rev.* B **65** 224112
[26] Cohen R E 1992 *High Pressure Research: Application to Earth and Planetary Sciences* ed Y Syono and M H Manghani (Washington, DC: Terra Scientific) p 425
[27] Kingma M J, Cohen R E, Hemley R J and Mao H K 1995 *Nature* **374** 243
[28] Karki B B, Warren M C, Stixrude L, Ackland G J and Crain J 1997 *Phys. Rev.* B **55** 3465
[29] Hohenberg P and Kohn W 1964 *Phys. Rev.* B **136** 864
[30] Kohn W and Sham L J 1965 *Phys. Rev.* A **140** 1133
[31] Payne M C, Teter M P, Allan D C, Arias T A and Joannopoulos J D 1992 *Rev. Mod. Phys.* **35** 1045
[32] Dovesi R, Saunders V R, Roetti C, Causà M, Harrison N M, Orlando R and Aprà E 1996 *Crystal98 User's Manual* (Turin: University of Turin)
[33] Ceperley D M and Alder B J 1980 *Phys. Rev. Lett.* **45** 566
[34] Burdett J K, Hughbanks T, Miller G J, Richardson J W and Smith J V 1987 *J. Am. Chem. Soc.* **109** 3639
[35] Gerward L and Olsen J S 1997 *J. Appl. Crystallogr.* **30** 259
[36] Isaak D G, Carnes D J, Anderson O L, Cynn H and Hake E 1998 *Phys. Chem. Miner.* **26** 31
[37] Kudoh Y and Takeda H 1986 *Physica* B **139/140** 333
[38] Hazen R M and Finger L W 1981 *J. Phys. Chem. Solids* **42** 143
[39] Porto S P S, Fleury P A and Damen T C 1967 *Phys. Rev.* **154** 522
[40] Eagles D M 1964 *J. Phys. Chem. Solids* **25** 1243
[41] See, for instance Srivastava G P 1990 *The Physics of Phonons* (Bristol: Hilger)
[42] Koudriachova M V, Harrison N M and de Leeuw S W 2002 *Phys. Rev.* B **65** 235423
Koudriachova M V, Harrison N M and de Leeuw S W 2002 *Comput. Mater. Sci.* **24** 235
[43] Ye X-S, Xiao Z-G, Lin D-S, Huang S-Y and Man Y-H 2000 *Mater. Sci. Eng.* B **74** 133
[44] Ashcroft N W and Mermin N D 1976 *Solid State Physics* (Orlando, FL: Harcourt College Publishers) p 548
[45] Woodley S M, Battle P D, Gale J D and Catlow C R A 1999 *Phys. Chem. Chem. Phys.* **1** 2535
[46] Isaak D G, Carnes J D, Anderson O L, Cynn H and Hake E 1997 *Phys. Chem. Miner.* **26** 31